

# EFFECT OF LOADING RATE ON HIGH-STRENGTH CONCRETE: NUMERICAL SIMULATIONS

MANUEL TARIFA\*, ELISA POVEDA, RENA C. YU,  
XIAOXIN ZHANG AND GONZALO RUIZ

Universidad de Castilla-La Mancha (UCLM)  
Avda. Camilo José Cela s/n, 13071 Ciudad Real, Spain  
\*e-mail: manuelagustin.tarifa@uclm.es, www.uclm.es

**Key words:** Drop-weight impact test, High-strength concrete, loading rate

**Abstract.** This paper is concerned with the numerical studies on the loading rate effect on the fracture behaviour of high-strength concrete. Numerical analysis has been carried out through employing ANSYS Parametric Design Language (APDL). Three-point-bend tests are simulated for six different loading rates, spanning seven orders of magnitude, from  $10^{-4}$  to  $10^3$  mm/s. In order to correctly capture the experimental results, two types of cohesive law, one for low loading rates and the other for high loading rates, both are dependent on the crack opening velocity, are implemented. The fitting parameters for both laws are given and the application range specified. In addition, by calculating the energy evolution, we are able to validate the hypothesis of Bathia *et al.* for measuring dynamic fracture energy. Finally, relevant information on crack advancing speed and opening velocity is also extracted and compared to available experimental data.

## 1 INTRODUCTION

Time-dependent fracture in normal-strength concrete (NSC) has been the focus of many researchers for several decades. It is commonly accepted that, according to Wu and Bazant [1], time-dependence of fracture is caused by three phenomena: (a) the inertia effect in the neighborhood of the crack-tip, (b) the rate dependence bond-breakage process which produces the fracture surfaces, and (c) viscoelastic behavior or creep in the bulk material. The third phenomenon is negligible for very fast dynamic fracture, whilst the first one is negligible for very slow and static fracture.

In respond to the little experimental data available [2–6] for rate-dependent fracture in high-strength concrete (HSC), Zhang *et al.* [7, 8] conducted an experimental campaign to examine the fracture behavior [7] and the crack advancing velocities from the bonded strain

gauges [8] on HSC from quasi-static to impact loading conditions. In this paper, we aim to reproduce these tests by employing ANSYS Parametric Design Language (APDL) and to numerically verify the hypothesis of Banthia *et al.* [9] for measuring dynamic fracture-energy.

The rest of the paper is structured as follows: the material characterization is presented in Section 2, the finite element method and the numerical analysis are described in Section 3, the results for these analysis are shown in Section 4 and finally the conclusions, obtained by this research, are depicted in Section 5.

## 2 MATERIAL CHARACTERIZATION

A high-strength concrete was used throughout the experiments of Zhang *et al.* [7, 8]. It was made with a Porphyry aggregate of 12 mm maximum size and ASTM type I cement, I 52.5R. Microsilica fume

slurry and super plasticizer (Glenium ACE 325, B225) were used in the concrete composition. The mixing proportions by weight were 1:0.187:2.12:0.445:0.30:0.065 (cement:water:coarse aggregate:sand:microsilica fume slurry:super plasticier). The mechanical properties, characterized through independent tests, are given in Table 1 and fed into the numerical model.

Table 1: Mechanical properties of the high-strength concrete, tested by Zhang *et al.* [7, 8].

	$f_c$ MPa	$f_t$ MPa	$G_F$ N/m	$E$ GPa	$\rho$ kg/m <sup>3</sup>
Mean	132	6.9	148	43	2700
St.D.	3	0.6	9	1	–

### 3 FINITE ELEMENT METHODOLOGY

In this section, we set out to model three-point-bend tests, using ANSYS APDL, a script language to automate common tasks and build complicated finite element models in terms of variables.

#### 3.1 Geometry and boundary conditions

Three-point-bend specimens tested are of 100×100 mm in cross section and 400 mm in total length, 300 mm in span, with a notch-depth ratio of 0.5. These specimen are discretized into two 8-node-volumetric-element groups (SOLID45), joined by pairs of contact elements (CONTA173 and TARGE170) in the crack propagation zone. The anti-torsion supports in the laboratory are modeled as unilateral boundary conditions represented by two contact elements (CONTA178) below the discretized specimen. Impact loads are applied to loading-line located at the center of the top surface, see Fig. 1.

The computational mesh comprises 10213 nodes and 3224 elements. It is designed to reduce the computational cost, so as to be fine in the vicinity of the crack propagation zone, with a size commensurate with the maximum aggregate size and to coarsen away from the crack propagation zone, see Fig. 1.

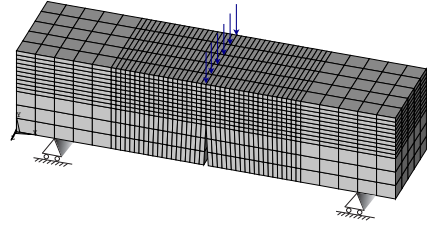


Figure 1: A typical FEM discretization and boundary conditions for a three-point-bend beam.

#### 3.2 Static analysis

Time-independent analysis is performed to determine loading-line displacement and stress distribution under static loading conditions. The analysis is employed to simulate the loading rate  $5.50 \times 10^{-4}$  mm/s, which is normally considered quasi-static.

The implemented static cohesive law, which relates the traction with the crack opening displacement  $w$ , according to the classical Hillerborg's Fictitious Crack Model [10], is formulated as follows

$$\sigma = f(w) \quad (1)$$

where  $f(w)$  is a general function of the opening displacement  $w$ , see Fig. 2c, where the shaded area quantifies the static fracture-energy  $G_F$ . A cohesive crack initiates when the stress at the crack-tip reaches the material tensile strength  $f_t$  and, its behavior is governed by Eq. 1 until a critical crack opening displacement  $w_c$  is reached.

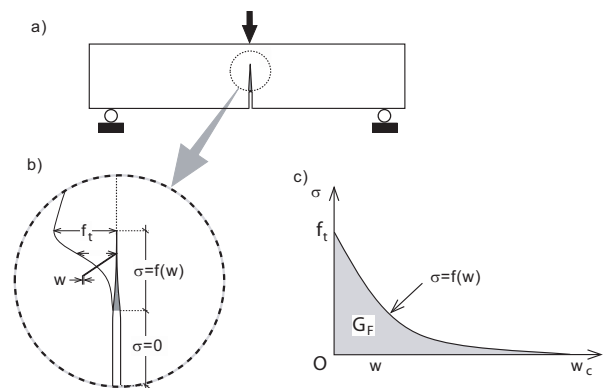


Figure 2: Static cohesive law representation.

### 3.3 Low loading rate analysis

Transient dynamic analysis is performed to simulate tests within the low loading rate range,  $5.50 \times 10^{-1}$  and  $1.74 \times 10^1$  mm/s. In order to correctly capture the strength increase of concrete with the variation in loading rate, a cohesive law with a viscous term, developed by Rosa *et al.* [11] and used by del Viso [12], is employed. This law is represented as follows:

$$\sigma(w, \dot{w}) = f(w) g(\dot{w}) \quad (2)$$

where  $g(\dot{w})$  is a stress intensification factor which depends on the crack opening velocity  $\dot{w}$ :

$$g(\dot{w}) = 1 + \left( \frac{\dot{w}}{\dot{w}_0} \right)^n \quad (3)$$

In the above equation  $\dot{w}_0$  is a normalization parameter with velocity dimensions, and  $n$ , the index of rate dependence, is a non-dimensional constant that describes the material viscosity degree. Both parameters are fitted to capture well the peak load for the two loading rates.

Figure 3 shows a viscous cohesive law, with a linear-decreasing shape for its static counterpart.

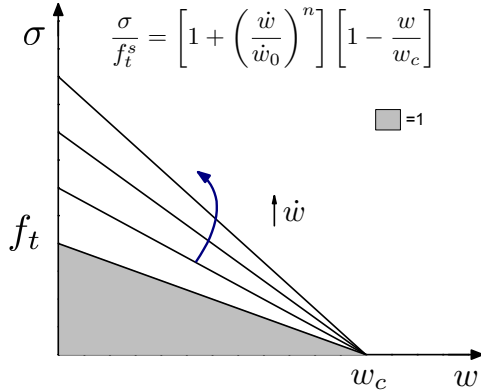


Figure 3: Viscous cohesive law representation.

### 3.4 High loading rate analysis

Three-point-bend tests under high loading rates ( $8.81 \times 10^2$ ,  $1.75 \times 10^3$  and  $2.65 \times 10^3$  mm/s) are simulated through a transient dynamic analysis.

Under low loading rates, the micro-cracking deformation is not significant and the main

crack propagates straight forward while, under high loading rates, many micro-cracks are developed within the crack tip zone because they lack time to unload each other. As a result, the dynamic fracture process happens in an enlarged damage zone that dissipates more energy. Zhou *et al.* [13] developed a cohesive law for high loading rates based on these micro-cracking process. In this law the increase of micro-cracking as a function of the loading rate [14, 15], produces a larger crack opening. The law is formulated as follows:

$$\sigma(w, \dot{w}) = f_t \left[ 1 - \frac{w}{h(\dot{w})w_c} \right] \quad (4)$$

where  $h$  is a crack opening intensification factor, represented as

$$h(\dot{w}) = 1 + \left( \frac{\dot{w}}{\dot{w}_o} \right)^m \quad (5)$$

where  $m$  describes the degree of micro-cracking. In Fig. 4, a simple cohesive law for high loading rate tests is depicted for different values of crack opening velocity.

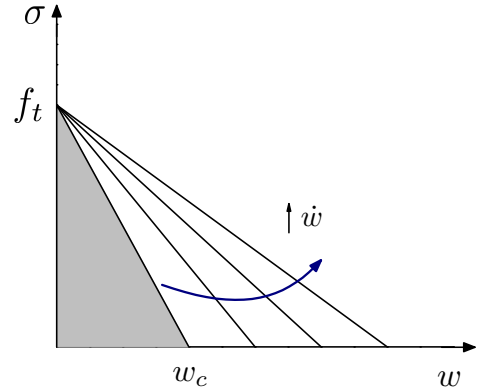


Figure 4: Cohesive law for high loading rate tests representation.

## 4 RESULTS AND DISCUSSION

In this section, we adopt the methodology described in Section 3 to simulate the three-point-bend tests carried out by Zhang *et al.* [7, 8]. These tests cover loading rates of seven orders of magnitude, they can be divided into two groups, the ones performed through the INSTRON machine (low loading rates) and the

ones through the Drop-weight impact machine (high loading rates) [16]. The lowest loading rate  $5.50 \times 10^{-4}$  mm/s, is considered as quasi-static, which is employed for material characterization of static properties in the laboratory.

First we show that the static cohesive law is able to correctly reproduce the entire load-displacement curve. Then we employ the viscous cohesive law to model the experimental results for low loading rates. For both cases, the peak loads are also contrasted with the analytical ones according to del Viso in [12].

Finally, the cohesive law shown in Eq. 4 is adopted for the tests at high loading rates, the evolution of energy is given to confirm the hypothesis of Banthia *et al.* [9] which is the basis for measuring dynamic fracture energy [7]. According to Banthia *et al.*, the reaction forces at the supports are the ones that break the specimen, consequently the energy below the reaction versus loading-line-displacement curve  $\mathcal{E}_B$ , see Fig. 5, is the true fracture energy.

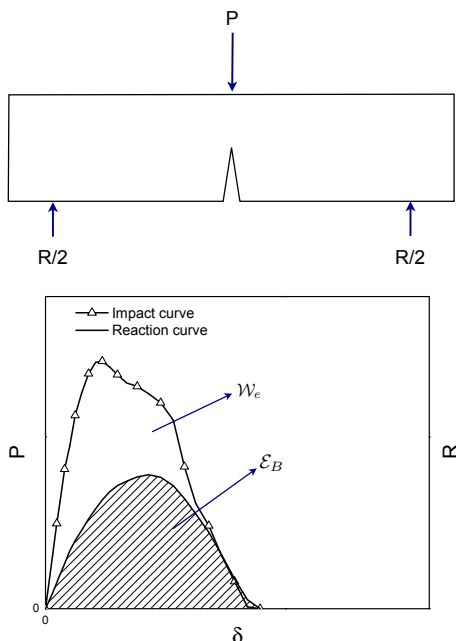


Figure 5: External work (or input energy) and the dynamic fracture energy in a dynamic three-point-bend test according to Banthia *et al.* [9].

#### 4.1 Static analysis

As mentioned before, tests performed at  $5.50 \times 10^{-4}$  mm/s are considered as quasi-static, therefore the static cohesive law is employed for their simulation. The numerical and experimental load versus loading-line-displacement curves are compared in Fig. 6. A good agreement is observed.

In addition, we plot the evolution for the strain energy  $\mathcal{E}_e$ , the fracture energy  $\mathcal{E}_F$  and the kinetic energy  $\mathcal{E}_k$  (remains zero throughout the loading process) in Fig. 7. The total energy  $\mathcal{E}_t$ , which is the sum of the three, is also contrasted with the external work  $\mathcal{W}_e$ .

In Table 2, we compare the peak load obtained from experimental measures, numerical and analytical calculations. The experimental and numerical results for fracture energy are also given.

Table 2: Experimental–numerical–analytical peak load and fracture energy comparison for the quasi-static case.

Loading rate (mm/s)	$P_{max}$ (kN)			$\mathcal{E}_F$ (J)	
	Exp.	Num.	An.	Exp.	Num.
$5.50 \times 10^{-4}$	5.0	4.8	5.0	0.7	0.6

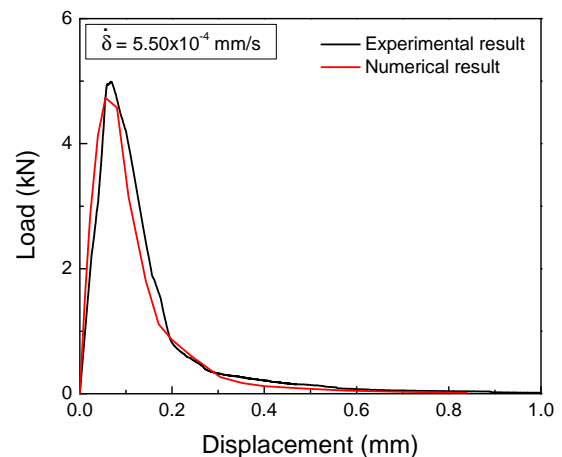


Figure 6: Comparison for the numerical and experimental quasi-static load-displacement curves.

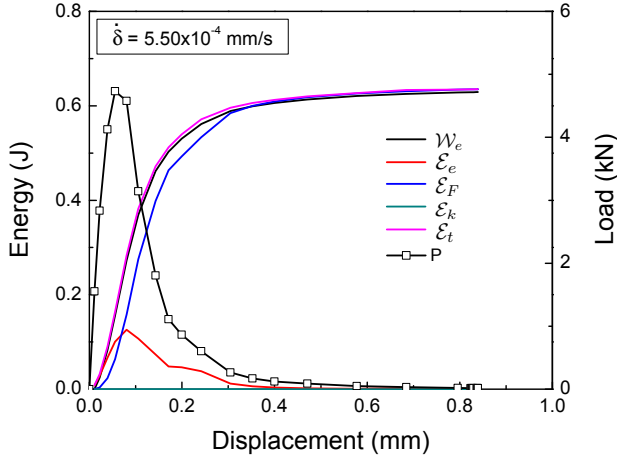


Figure 7: Modelled energy evolution contrasted with the load history for the quasi-static case.

#### 4.2 Low loading rate analysis

The viscous cohesive described in Eq. 2 is employed to model the tests at two low loading rates. The parameters that give the best fit are as follows

$$n = 0.16, \quad w_0 = 30 \text{ mm/s} \quad (6)$$

For demonstration purpose, we show the numerical and experimental load-displacement curves for the loading rate  $5.50 \times 10^{-1}$  mm/s in Fig. 8, the corresponding energy evolution in Fig. 9. Note that, the accumulated strain energy reaches its maximum at peak load; after that the external work is mainly spent on crack propagation.

Table 3: Experimental–numerical–analytical  $P_{max}$  and  $\mathcal{E}_F$  comparison for tests at low loading rates.

Loading rate (mm/s)	$P_{max}$ (kN)			$\mathcal{E}_F$ (J)	
	Exp.	Num.	An.	Exp.	Num.
$5.50 \times 10^{-1}$	7.3	7.9	6.4	1.1	0.8
$1.74 \times 10^1$	8.0	8.4	7.7	1.1	1.0

The exact cohesive law followed is depicted in Fig. 10 for the loading rate of

$1.74 \times 10^1$  mm/s. Notice that, the viscous effect leads to hardening of the material at the beginning of the crack opening, and gradual softening as the crack opens up. When the external load is plotted against the crack opening at the crack tip, see Fig. 10(bottom), we observe that a stress free crack has formed at the notch tip, since the critical opening displacement  $w_c$  is reached when the load drops to 6.5 kN.

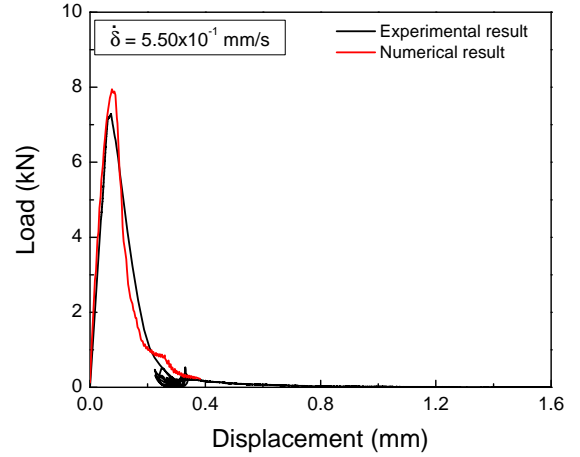


Figure 8: Numerical and experimental load-displacement curves for the loading rate  $5.50 \times 10^{-1}$  mm/s.

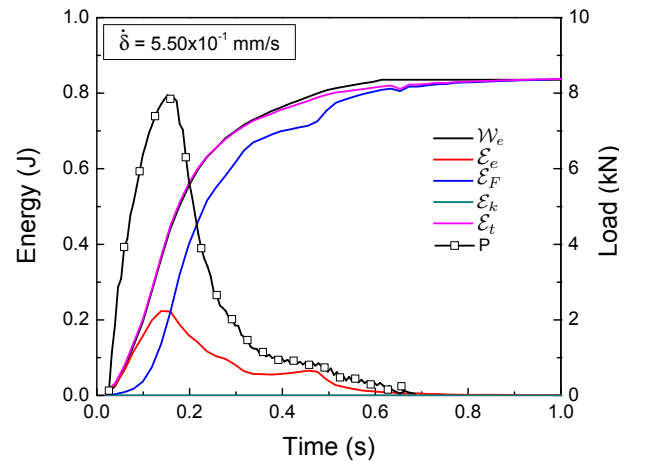


Figure 9: Modelled energy evolution contrasted with the load history for the loading rate of  $5.50 \times 10^{-1}$  mm/s.

### 4.3 High loading rate analysis

The cohesive of Zhou *et al.* [13] described in Eq. 4 is implemented to simulate the tests at high loading rates. The two parameters that give best fit are as follows

$$m = 0.24, \quad w_0 = 9 \times 10^{-6} \text{ mm/s} \quad (7)$$

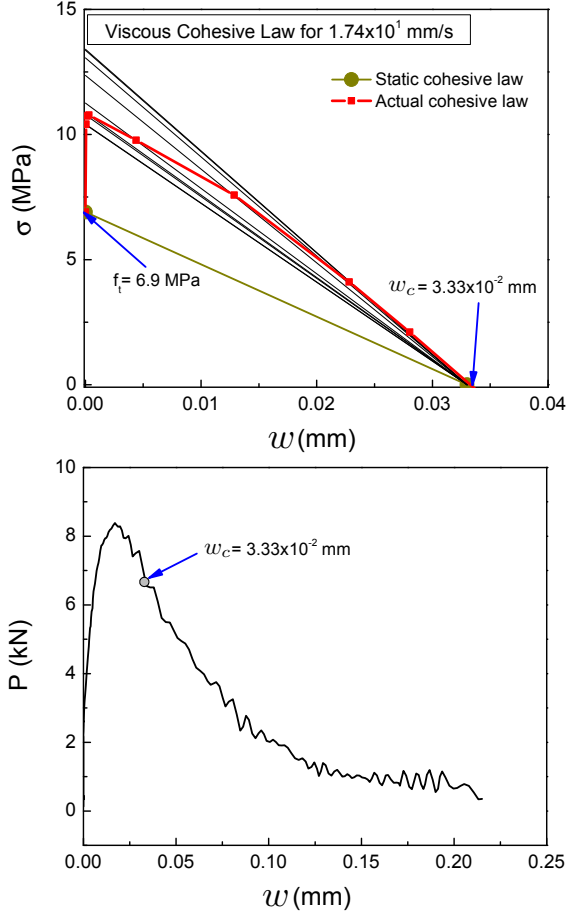


Figure 10: Viscous cohesive law evolution (top) and the external load (bottom) plotted against the crack opening at the notch tip for a loading rate of  $1.74 \times 10^1$  mm/s.

The experimental and numerical comparison for peak load  $P_{max}$  and fracture energy  $\mathcal{E}_F$  is shown in Table 4. Meanwhile, the load-displacement curves and modelled energy evolution are illustrated in Fig. 11 and Fig. 12 for the loading rate  $2.65 \times 10^3$  mm/s. Additionally plotted in Fig. 12 are the evolutions of load and reaction forces with respect to time. It

is noteworthy that the accumulated kinetic energy reaches maximum when the sum of reaction force at the two supports reaches its peak. At the end of the calculation, even though there are still considerable amount of kinetic energy left, the consumed fracture energy approaches the energy of Bantia, which is the shaded area shown in Fig. 5. In other words, with the applied numerical model, we have confirmed that, the area shown in Fig. 5 can indeed represent the expenditure of the dynamic fracture energy at high loading rates.

Table 4: Experimental–numerical  $P_{max}$  and  $\mathcal{E}_F$  comparison for the high loading rate range.

Loading rate (mm/s)	$P_{max}$ (kN)		$\mathcal{E}_F$ (J)	
	Exp.	Num.	Exp.	Num.
$8.81 \times 10^2$	21.7	23.2	6	4
$1.75 \times 10^3$	34.8	39.9	17	16
$2.65 \times 10^3$	45.7	53.7	29	28

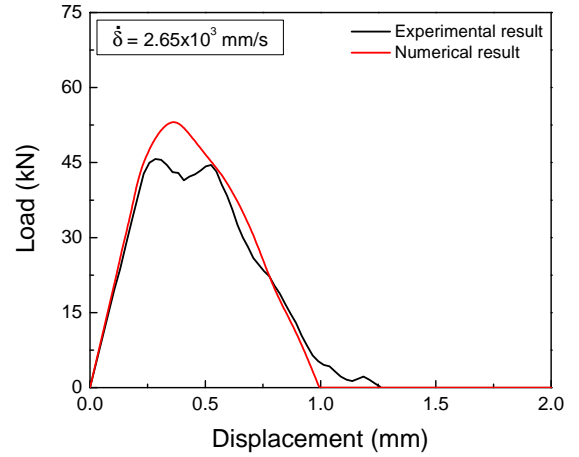


Figure 11: Numerical and experimental load-displacement curves for the loading rate  $2.65 \times 10^3$  mm/s.

We represent the actual cohesive law for the loading rate of  $2.65 \times 10^3$  mm/s in Fig. 13. It needs to be pointed out that, the larger crack opening (in comparison with its static counterpart) simulated in Fig. 13 is an equivalent representation for the increase of micro-cracking,

since only a single crack is allowed to propagate. When contrasted with the reaction force versus crack opening at the notch tip, we observe that, the cohesive crack continues to grow after the reaction force has reached zero.

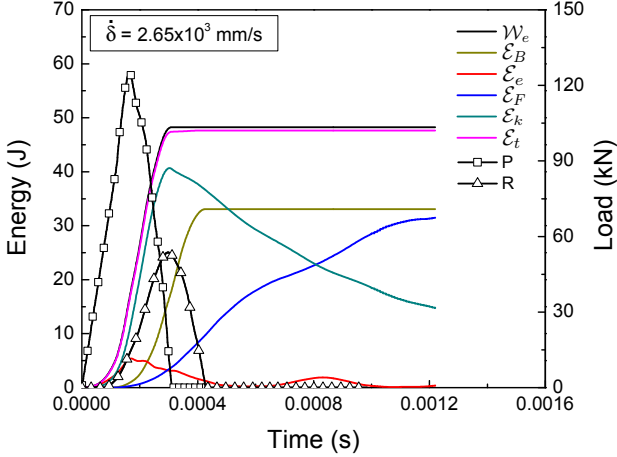


Figure 12: Modeled energy evolution contrasted with the load and reaction force histories for the loading rate  $2.65 \times 10^3$  mm/s.

#### 4.4 Application range of the cohesive laws

In this section, we study the application range for the two cohesive laws mentioned above. For this purpose, we apply the two cohesive laws in Eq. 2 and Eq. 4 with their corresponding parameters in Eq. 6 and Eq. 7 for the transitional loading rates between  $1.74 \times 10^1$  mm/s and  $8.81 \times 10^2$  mm/s. For an error below 5%, the common range for both laws to apply is between  $4.40 \times 10^2$  mm/s and  $5.20 \times 10^2$  mm/s, see Fig. 14.

#### 4.5 Loading rate effect on crack advancing and opening velocities

From the established numerical model, we calculate both the crack advancing speed and the crack opening velocity. The crack advancing speed compared to experimental measurements for the loading rate  $1.74 \times 10^1$  mm/s and  $1.75 \times 10^3$  mm/s are given in Fig. 15 and Fig. 16 respectively; whereas the numerical crack opening velocities are presented in Fig. 17.

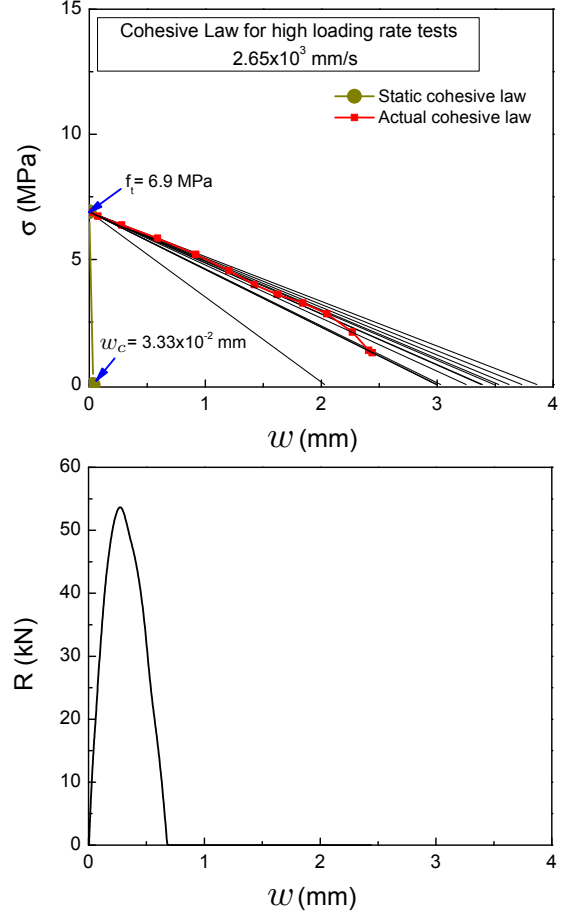


Figure 13: Cohesive law evolution (top) and the reaction force plotted against the crack opening at the notch tip for the loading rate  $2.65 \times 10^3$  mm/s.

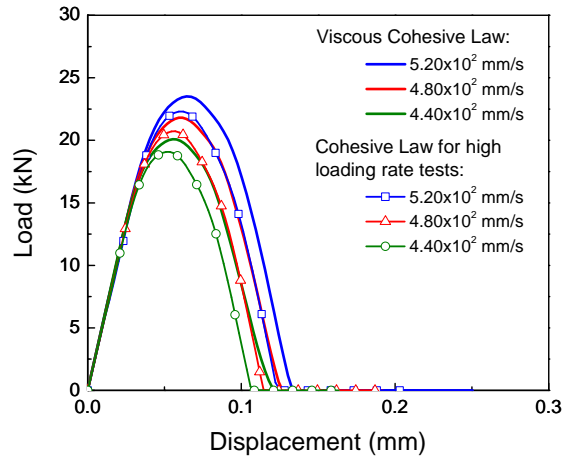


Figure 14: Load versus displacement curves simulated by the cohesive laws in Eq. 2 and Eq. 4.

From Fig. 15 and Fig. 16, it can be observed that, even though the numerical results predict lower maximum crack advancing speed, i.e. 8 m/s instead of 16 m/s for the loading rate  $1.74 \times 10^1$  mm/s, 300 m/s instead of 400 m/s for the loading rate  $1.75 \times 10^3$  mm/s, the order of magnitude is correctly captured.

From Fig. 17b and Fig. 17c, the crack opening velocity evolution with respect to time at each node starts with a linear branch and reaches a constant stage after peak load. This is attributed to the weigh compensation technique employed to attain a stable crack propagation for the low loading rate tests. Note that, the crack opening velocity at the notch tip, node 3, reaches 20 mm/s, which is the same order of the applied loading rate.

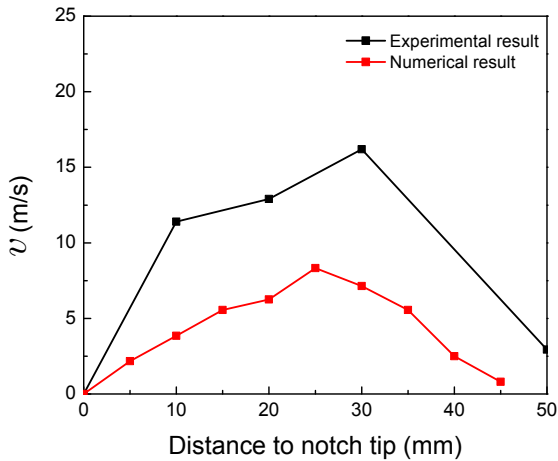


Figure 15: Crack advancing velocities for the loading rate  $1.74 \times 10^1$  mm/s.

For the case of high loading rate  $1.75 \times 10^3$  mm/s, see Fig. 17d and Fig. 17e, the crack opening velocity evolution has a smoother profile, a clear peak velocity is also observed. In particular, at the notch tip, node 3, opening velocity reaches 2 m/s, which is also the same order of the applied loading rate.

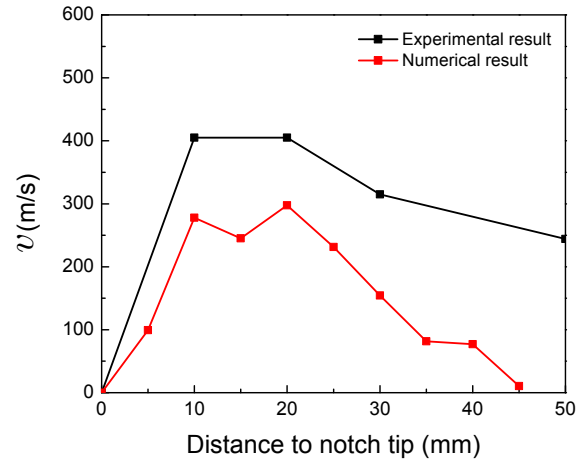


Figure 16: Crack advancing velocities for the loading rate  $1.75 \times 10^3$  mm/s.

## 5 CONCLUSIONS

We have implemented two cohesive laws to model three-point-bend tests carried out at loading rates which cover seven orders of magnitude. In particular, the viscous cohesive law proposed by Rosa *et al.* [11] captures well the experimental tests carried out at low loading rates; whereas the one developed by Zhou *et al.* [13], reproduces well those tests performed at high loading rates. Fitting parameters for both laws are given and the application range specified. From the energy evolution simulated for the tests at high loading rates, we have confirmed that the hypothesis of Bantia *et al.* [9] for measuring dynamic fracture energy is valid, at least for the beam geometry studied in this current work.

Finally, we have extracted both the crack advancing and crack opening velocities for all loading rates. The former ones compare well with available experimental measurements, whereas the latter ones show the same order of magnitude as the corresponding loading rates.

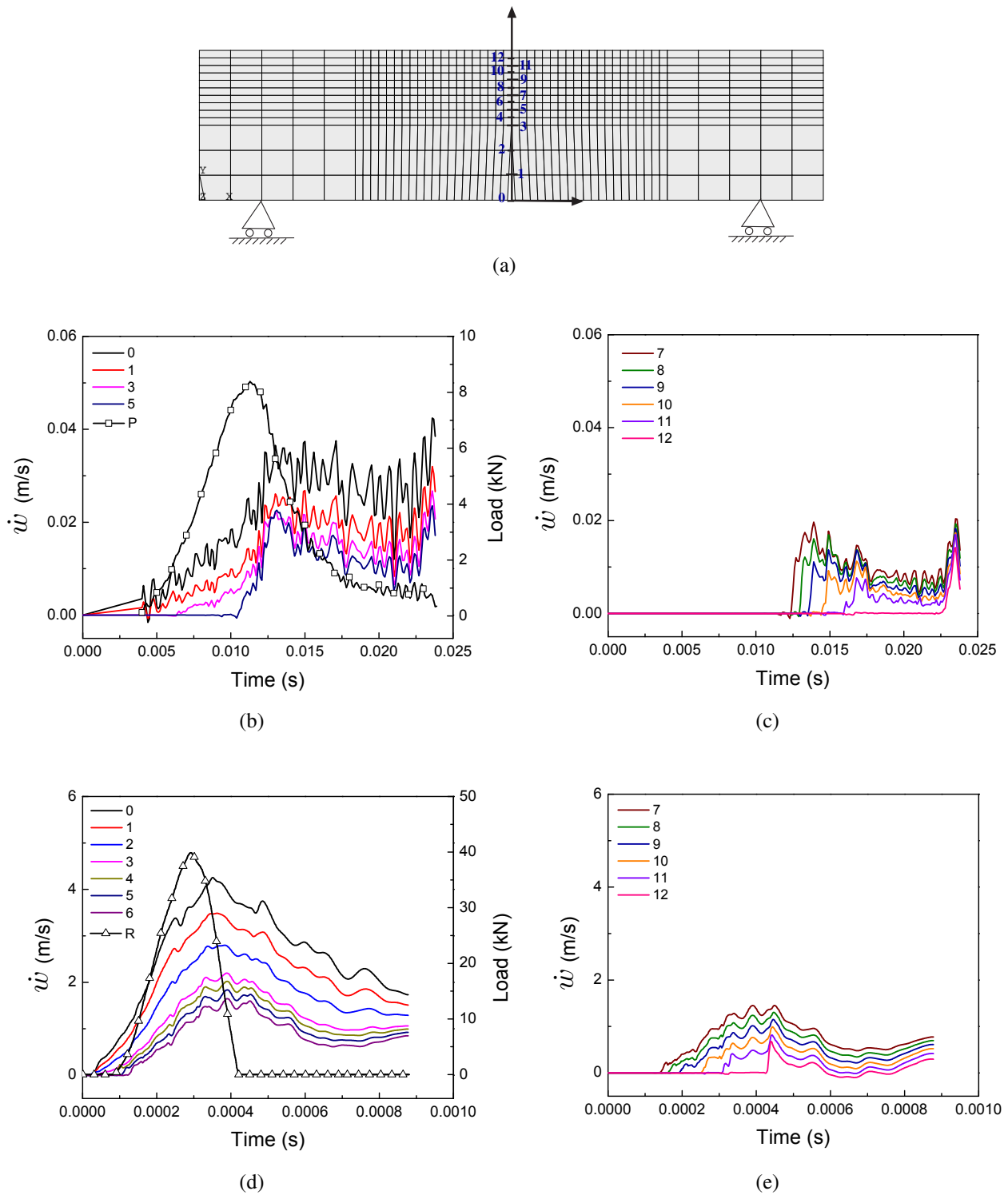


Figure 17: a) Position of the 13 nodes where the crack opening velocities are calculated; and crack opening velocities contrasted with load or reaction history for loading rates  $1.74 \times 10^1$  mm/s (b-c) and  $1.75 \times 10^3$  mm/s (d-e).

## Nomenclature

- $\mathcal{W}_e$ : External work (or input energy).
- $\mathcal{E}_k$ : Kinetic energy.
- $\mathcal{E}_e$ : Elastic strain energy.
- $\mathcal{E}_F$ : Fracture energy.
- $\mathcal{E}_t$ : Total energy ( $\mathcal{E}_k + \mathcal{E}_e + \mathcal{E}_F$ ).
- $\mathcal{E}_B$ : Energy calculated according to the hypothesis of Bantia (dynamic fracture energy).
- $P$ : Applied external load.
- $R$ : Reaction force.
- $P_{max}$ : Peak load.
- $\delta$ : Loading-line displacement.
- $\dot{\delta}$ : Loading-line displacement rate.
- $v$ : Crack advancing speed.
- $w$ : Crack opening.
- $\dot{w}$ : Crack opening velocity.

## REFERENCES

- [1] Wu, Z.S. and Bazant, Z.P., 1993. Finite element modeling of rate effect in concrete fracture with influence of creep. In Bazant and Carol, editors. "Creep and shrinkage of concrete". *Proceedings of the fifth international RILEM symposium*.
- [2] Hu, X.Z. and Wittmann, F.H., 1990. Experimental method to determine extension of fracture process zone. *Journal of Materials in Civil Engineering*, **2**: 15-23.
- [3] Comité Euro international du Béton, 1995. State of the art report, high strength concrete, Recommended extensions to the Model Code 90, Research needs. *CEB Bulletin d'Information*, **228**.
- [4] Müller, H., 2008. Constitutive modelling of high strength/high performance concrete-state of the art report. *CEB FIP Bulletin*, **42**.
- [5] Ruiz, G., Zhang, X.X., Yu, R.C., Porras, R., Poveda, E. and del Viso, J.R., 2011. Effect of loading rate on fracture energy of high-strength concrete. *Strain*, **47(6)**: 518-524.
- [6] Zhang, X.X., Ruiz, G., Yu, R.C., Poveda, E. and Porras, R., 2012. Rate effect on the mechanical properties of eight types of high-strength concrete and comparison with FIB MC2010. *Construction and Building Materials*, **30**: 301-308.
- [7] Zhang, X.X., Ruiz, G., Yu, R.C. and Tarifa, M., 2009. Fracture behavior of high-strength concrete at a wide range of loading rates. *International Journal of Impact Engineering*, **36**: 1204-1209.
- [8] Zhang, X.X., Yu, R.C., Ruiz, G., Tarifa, M. and Cmara, M.A., 2010. Effect of loading rate on crack velocities in HSC. *International Journal of Impact Engineering*, **37(4)**: 359-370.
- [9] Bantia, N., Mindess, S., Bentur, A. and Pigeon, M., 1989. Impact testing of concrete using a drop-weight impact machine", *Experimental Mechanics*, **29(1)**: 63-69.
- [10] Hillerborg, A., Modeer, M., 1976. Analysis of crack formation and crack growth in concrete by means of fracture mechanics and finite elements. *Cement and Concrete Research*, **6**: 773-782.
- [11] Rosa, A.L., Yu, R.C., Ruiz, G., Saucedo, L. and Sousa, J.L.A.O., 2012. A loading rate dependent cohesive model for concrete fracture. *Engineering Fracture Mechanics*, **82**: 195-208.
- [12] Del Viso, J.R., 2008. Comportamiento mecánico en fractura del hormigón de alta

- resistencia y su variación con la velocidad de sollicitación. *PhD Thesis*, Universidad de Castilla-La Mancha, Ciudad Real.
- [13] Zhou, F., Molinari, J.F. and Shioya, T., 2005. A rate-dependent cohesive model for simulating dynamic crack propagation in brittle materials. *Engineering Fracture Mechanics*, **72**: 1383-1410.
- [14] Brara, A. and Klepaczko, J. R., 2007. Fracture energy of concrete at high loading rates in tension. *International Journal of Impact Engineering*, **34(3)**: 424-435.
- [15] Vegt, I., Breugel, K. V. and Weerheijm, J., 2007. Failure mechanisms of concrete under impact loading. In Carpinteri, A., Gambarova, P.G., Ferro, G. and Plizzari, G.A. *Fracture Mechanics of Concrete and Concrete Structures*, **1-3**, Catania, Italy, Jun 17-22, 2007.
- [16] Zhang, X.X., Ruiz, G. and Yu, R.C., 2010. A new drop-weight impact machine for studying fracture processes in structural concrete. *Strain*, **46(3)**: 252-257.
- [17] Rossi, P. and Toulemonde, E., 1996. Effect of loading rate on the tensile behavior of concrete: description of the physical mechanisms, *Materials and Structures*, **29(186)**: 116-118.
- [18] Camacho, G.T., Ortiz, M., 1996. Computational modelling of impact damage in brittle materials. *International Journal of Solids and Structures*, **33**: 2899-2938.
- [19] Yu, R.C., Zhang, X.X., Ruiz, G., 2008. Cohesive modeling of dynamic fracture in reinforced concrete, *Computers and Concrete*, **5(4)**: 389-400.